Applied Catalysis B: Environmental 271 (2020) 118938

Contents lists available at ScienceDirect

Applied Catalysis B: Environmental

journal homepage: www.elsevier.com/locate/apcatb

Highly efficient methane decomposition to H_2 and CO_2 reduction to CO via redox looping of $Ca_2Fe_xAl_{2-x}O_5$ supported $Ni_yFe_{3-y}O_4$ nanoparticles

Zhao Sun[a,b], Tianyi Cai[c,d], Christopher K. Russell[e], J. Karl Johnson[d], Run-Ping Ye[b], Wenguo Xiang[c], Xiaoping Chen[c], Maohong Fan[b,f,*], Zhiqiang Sun[a,**]

[a] School of Energy Science and Engineering, Central South University, Changsha, 410083, China
[b] Departments of Chemical and Petroleum Engineering, University of Wyoming, Laramie, WY, 82071, USA
[c] Key Laboratory of Energy Thermal Conversion and Control of Ministry of Education, School of Energy and Environment, Southeast University, Nanjing, 210096, China
[d] Department of Chemical & Petroleum Engineering, Swanson School of Engineering, University of Pittsburgh, Pittsburgh, PA, 15261, USA
[e] Davidson School of Chemical Engineering, Purdue University, West Lafayette, IN, 47907, USA
[f] School of Civil and Environmental Engineering, Georgia Institute of Technology, Atlanta, GA, 30332, USA

ARTICLE INFO

Keywords:
Methane decomposition
Hydrogen production
CO_2 reduction
Chemical looping
$Ni_yFe_{3-y}O_4$ nanoparticles

ABSTRACT

Catalytic methane decomposition (CMD) due to its various potentials including production of CO_x free H_2 and technically simpleness, but is very challenging due to the lack of efficient, stable, and carbon-separable catalysts. An innovative chemical looping methane decomposition with CO_2 reduction (CLMDCR) was developed to bridge the gap via the reduction → CMD → oxidation looping of a catalytic oxygen carrier (COC) for H_2 production, deposited carbon separation, and CO_2 reduction to CO. As high as 96.3 vol.% and 95.2 vol.% purities of H_2 and CO can be generated using the COC ($Ni_yFe_{3-y}O_4$-$Ca_2Fe_xAl_{2-x}O_5$), superior to those obtained with state-of-the-art CH_4 dry reforming. The COC shows not only high activities but also remarkable durability as demonstrated with 20 cyclic CLMDCR tests. Experimental results indicate that the long-term redox durability of COC is attributed to its atomic homogenization through the phase transformations of $Ni_yFe_{3-y}O_4$ ↔ Ni-Fe and $Ca_2Fe_{1.52}Al_{0.48}O_5$ ↔ CaO + Fe + $Ca_2Fe_xAl_{2-x}O_5$.

1. Introduction

Hydrogen is a promising energy carrier due to its efficiency and lack of CO_2 generation when utilized [1,2]. Currently, H_2 is mainly produced via steam reforming of natural gas, requiring costly and complicated separations [3,4]. For this reason, simple and efficient methods of H_2 generation are of significant interest [5,6]. Catalytic methane decomposition (CMD) is a promising method for producing H_2 due to its advantages, including simplicity, low temperature need enabled with catalysts, near zero CO_x gas emission, almost-pure H_2 production without using steam, CO_2, or O_2 [7–10], and production of sole by-product (value-added nano-carbon). Methane decomposition is moderately endothermic, requiring temperatures above 1000 °C to break the strong C–H bond of CH_4 at an acceptable decomposition rate when uncatalyzed [11,12]. Hence, a variety of metal catalysts have been investigated for lowering the temperature required for methane decomposition while maintaining the CH_4 conversion rate. Iron (Fe), cobalt (Co), and nickel (Ni) have shown high catalytic activities in methane activation [13–18]. In particular, Ni-based catalysts have been identified as a promising choice for CMD in a moderate temperature range [19], and their performances during CMD highly depend on their sizes and crystallinities [20,21]. Additionally, their decomposition activity and the durability without using supporting materials decline rapidly, resulting from their sintering, agglomeration, as well as encapsulation [21].

To overcome the challenges of the catalysts, support materials such as Al_2O_3, SiO_2, MgO, TiO_2, SiO_2, and ZrO_2 were normally used to promote the dispersion of active metals on the support and enhance their CMD [22]. Ashik et al. [11] compared the activities and stabilities of nano Ni/SiO_2, Fe/SiO_2, and Co/SiO_2 during CMD. The performances in terms of their activities and stabilities are in the order of Ni/SiO_2 > Co/SiO_2 > Fe/SiO_2 and the achieved maximum methane conversion is 64.4 %. Kang et al. [23] synthesized Ni-carbon-B_2O_3 nanocomposites and investigated their CMD performance. These catalysts achieved 90 % methane conversion with 61 mmol min^{-1} gNi^{-1} at 850 °C. Pudukudy et al. [21] synthesized Ni/MgO and Fe/MgO catalysts

* Corresponding author at: Departments of Chemical and Petroleum Engineering, University of Wyoming, Laramie, WY, 82071, USA.
** Corresponding author.
E-mail addresses: mfan@uwyo.edu (M. Fan), zqsun@csu.edu.cn (Z. Sun).

https://doi.org/10.1016/j.apcatb.2020.118938
Received 3 December 2019; Received in revised form 22 March 2020; Accepted 24 March 2020
Available online 30 March 2020
0926-3373/

via a one-pot sol-gel method and evaluated their CMD performances within 700 − 900 °C. They found that Fe/MgO was better than Ni/MgO. No catalyst deactivation was observed within 360 min reaction [21]. Rastegarpanah et al. [24] also investigated the influence of group VIB metals (Cr, Mo, and W) on the activity of Ni/MgO catalysts during methane decomposition. Results indicate that the Cr-doped Ni/MgO samples show high catalytic efficiency due to its high surface area, high oxygen adspecies concentration, and satisfied low-temperature reducibility. In addition, many Ni-based alloys such as Ni-Pt, Ni-Pd, Ni-Co, Ni-Cu, and Ni-Mo were also studied to improve CMD performance [25–30].

Despite the intensive research on CMD, there are still many unresolved challenges. These include separation of H_2 from impurities in the product stream, separation of the catalyst from deposited carbon, and utilization of the produced carbon materials. The study from Chen et al. [31] indicate that the deactivation of the catalyst (electroless nickel plating) was attributed to the coking which leads to the loss of catalyst's active sites. Thus, it is significant to remove the deposited carbon after a suitable period of methane decomposition time, achieving the catalyst regeneration. For catalyst regeneration, O_2, CO_2, and steam can be utilized to oxidize the deposited carbon. Lim et al. [32] conducted a chemical looping-based methane reforming-decomposition process with CO_2 conversion, in which CO_2 and O_2 were successively utilized for converting CO_2 to CO as well as achieving coke gasification. However, the oxygen involved deposited carbon combustion may cause the excessive of local temperature, exacerbating the sintering and agglomeration of the catalyst and thus resulting in the deactivation of the catalyst. Carbon dioxide is a mild oxidizer and its use during catalyst regeneration leads to the production of almost pure CO [23].

Chemical looping offers a compelling alternative for effective conversion of carbonaceous fuel into clean energy carriers or value-added chemicals through redox looping of an oxygen carrier [33,34]. Accordingly, integration of chemical looping with methane decomposition process with CO_2 reduction (CLMDCR) to address above-mentioned concerns associated with state-of-the-art CMD is of significant interest, and has rarely been reported. Further, the development of a highly efficient and multifunctional looping agent is a key issue for CLMDCR process. Thus, we aim at demonstrating the ability of CLMDCR to efficiently produce high-purity H_2 from methane decomposition and CO_2 reduction to CO using a dual-functional material we denote as CFAN ($Ni_yFe_{3-y}O_4$-$Ca_2Fe_xAl_{2-x}O_5$). $Ni_yFe_{3-y}O_4$ is designed to generate a Ni-Fe alloy during CH_4 reduction and the selection of $Ca_2Fe_xAl_{2-x}O_5$ is to disperse the active components and provide acidic sites for promoting methane conversion. CFAN acts both as an oxygen carrier for redox looping, and an active catalyst for CMD in its reduced state, thus we name it as catalytic oxygen carrier (COC). The proposed CLMDCR process utilizes CO_2 as an oxidizing agent, achieving a net reduction of CO_2 together with the re-oxidation of CFAN and the separation of deposited carbon from CFAN. The main product from CO_2 reduction is CO, which can be used for the methanol, acetic acid, and other carbonylation reactions [35–38]. Moreover, the CFAN's performances including catalytic activity, particle morphology evolution, cyclic stability, and the ability to inhibit sintering and agglomeration were thoroughly discussed.

2. Experimental procedures

2.1. COC preparation

Calcium nitrate tetrahydrate (> 99 %), iron nitrate nonahydrate (ACS reagent, > 98 %), cerium nitrate hexahydrate (99 % trace metal basis), nickel nitrate hexahydrate (99.999 % trace metals basis), and citric acid (ACS reagent, > 99.5 %) were obtained from Sigma-Aldrich and Aluminum nitrate nonahydrate (> 98 %) was used as received from Alfa Aesar. All the COCs were prepared by a modified Pechini synthesis described in previous works [2,5,39]. In a typical procedure for preparing $Ni_yFe_{3-y}O_4$-$Ca_2Fe_xAl_{2-x}O_5$, $Ca(NO_3)_2{\cdot}4H_2O$, $Fe(NO_3)_3{\cdot}9H_2O$, $Al(NO_3)_3{\cdot}9H_2O$, $Ni(NO_3)_2{\cdot}6H_2O$, and citric acid (mole ratio Ca: Fe: Al: Ni: citric acid = 4: 4: 1: 1: 20, $Fe(NO_3)_3$ 0.1 M) were dissolved in deionized water while stirring constantly for 30 min at room temperature. The resulting solution was dried at 180 °C for 12 h. The sample was then calcined at 850 °C with a heating rate of 2.5 °C /min and four-hour dwell time. Six COCs, Ca-Fe, Ca-Fe-Al, Ca-Fe-Ce, Ca-Fe-Ni, Ca-Fe-Al-Ce, and Ca-Fe-Al-Ni (abbreviated as CF, CFA, CFC, CFN, CFAC, and CFAN) were prepared using the same preparation methods. The nominal atomic ratio of the samples is provided in Table S1.

2.2. Characterization

The metal content in each COC was determined by inductively coupled plasma optical emission spectroscopy (ICP-OES, 7700x, Agilent). X-ray diffraction (XRD) measurements were performed by a Rigaku Smartlab X-ray diffractometer using Cu Kα (λ = 1.5406 Å) radiation 40 kV and 40 mA operated on continuous scan mode. The X-ray diffraction was recorded in a range of 20 − 80° at a scan rate of 8°/min with a step of 0.02°. N_2 adsorption and desorption isotherms at − 196 °C were measured using an automatic Quantachrome instrument after evacuation at 200 °C for 6 h. The BET surface area was determined from nitrogen adsorption data within the relative pressure range of 0.01 − 0.3. The pore size distribution was obtained via the Barret-Joyner-Halenda (BJH) method, and total pore volume was determined from nitrogen adsorption at a relative pressure of 0.99. Raman spectra of generated carbon were recorded in triplicate using a Sierra IM-52 portable Raman spectrometer with a 532 nm laser beam and 5 mW laser with 15-second integration time.

To determine the chemical states of as-prepared and reacted CFAN surface, X-ray photoelectron spectroscopy (XPS) was carried out using a Thermo-scientific ESCALAB 250 instrument with a monochromatic Al Kα X-ray source with spot size 500 μm. Survey and composition scans were conducted using a pass energy of 150 and 20 eV, respectively, using low-energy electron flooding for charge neutralization. The binding energy scales were calibrated with C_{1s} (284.8 eV). Scanning electron microscopy (SEM) was performed using a FEI Quanta FEG 450 scanning electron microscope to characterize the morphology of the samples after methane decomposition. The Ca, Fe, Al, and Ni distributions were investigated using energy dispersive spectroscopy (EDS). The microstructure of the as-prepared, reacted, and cycled samples was characterized by Transmission electron microscopy (TEM) and scanning transmission electron microscopy (STEM) using a FEI Titan 80–300 S-Twin transmission electron microscope equipped with a spherical aberration image corrector at 300 kV and a retractable EDX detector. The TEM-EDX mapping was collected at 300 kV using a beam current of 1 nA.

H_2 temperature-programmed reduction (H_2-TPR) measurements were carried out in a Quantachrome TP_x automated gas sorption analyzer. For each experiment, 0.10 g sample was put into a quartz reactor and was out-gassed by helium at 150 °C for 30 min. The sample was then cooled to 30 °C followed by flowing 5% H_2 in N_2 over the surface for 60 min. After that, the temperature was ramped from 30 to 1050 °C with a heating rate of 5 °C/min. Temperature programmed oxidation (CO_2-TPO) measurements were carried out by an SDT Q600 thermogravimetric analyzer (TGA) to test the CO_2 oxidation performance of the reacted samples. Typically, a small amount of reacted sample (~10 mg COCs, obtained from CH_4 decomposition at 750 °C in 20 vol.% CH_4 in N_2 for 2 h) was placed in an alumina crucible and heated to 1000 °C at 10 °C/min under 50 mL/min of 20 vol.% CO_2 in N_2.

2.3. Catalytic test

Thermogravimetric analysis (TGA, TA Instrument, SDT Q600) was

used for COC (CF, CFA, CFC, CFN, CFAC, and CFAN) screening. In a typical activity test, 10.0 ± 1.0 mg sample was heated at 10 °C/min to 750 °C in 40 mL/min N_2. After temperature stabilization, 50 mL/min of 20 vol.% CH_4 in N_2 flowed over the samples for 35 min. To prevent the direct contact of CH_4 and CO_2, N_2 purging (10 min) was simultaneously conducted while the system was heated from 750 to 800 °C at a heating rate of 5 °C/min. After that, carbon oxidation/COC regeneration were performed under 10 mL/min 20 vol.% CO_2 in N_2 for 75 min. All the gas switching was performed by the mass flow controllers and controlled by the software LabVIEW.

Catalytic activity, product selectivity, and cyclic stability of the samples were studied in a fixed bed reactor. The experimental system was composed of an electrical furnace with a temperature controller, a quartz tube reactor (Length 600 mm, ID 10 mm, OD 13 mm), flow meters, and a gas chromatograph at the outlet of the reactor. In a typical methane decomposition test, 0.200 ± 0.005 g sample was loaded in the quartz tube reactor. The system was purged with N_2 for 20 min before the furnace was heated from room temperature to the desired temperature (600 °C, 650 °C, 700 °C, 750 °C, 800 °C, or 850 °C, 10 °C/min) in 40 mL/min N_2. Upon temperature stabilization, the sample was reacted in 50 mL/min flow gas (20 vol.% CH_4 in N_2) for 30 min, 60 min, or 120 min. After 30 min of purging while adjusting the temperature, CO_2 reduction experiments were performed using reacted samples from methane decomposition experiments at a specific temperature (750 °C, 800 °C, 850 °C, or 900 °C) under 50 mL/min flow gas (20 vol.% CO_2 in N_2). This cycle is then repeated according to the following protocol: 30 min CH_4 decomposition → 30 min N_2 purge → 60 min CO_2 reduction → 30 min N_2 purge. The concentration of the gas products was determined by an INFICON Micro GC TCD detector.

Reactant conversion, production rate, and product selectivity for species 'x' are denoted by X(x), P(x), and S(x), respectively, and are defined as:

$$X(CH_4) = \frac{R(CH_4, in) - R(CH_4, out)}{R(CH_4, in)} \quad (1)$$

$$X(CO_2) = \frac{R(CO_2, in) - R(CO_2, out)}{R(CO_2, in)} \quad (2)$$

$$P(H_2) = \frac{P(N_2) \times C(H_2)}{C(N_2)} \quad (3)$$

$$P(CO) = \frac{P(N_2) \times C(CO)}{C(N_2)} \quad (4)$$

$$S(H_2) = \frac{P(H_2)}{2R(CH_4, in)\text{-}2R(CH_4, out)} \quad (5)$$

$$S(CO) = \frac{P(CO)}{R(CO_2, in) - R(CO_2, out)} \quad (6)$$

where C(x) represents the outlet mole fraction of x (x = N_2, H_2, or CO), and R(y, in) and R(y, out) are the feed and production rate of y (y = CH_4 or CO_2), respectively.

2.4. Computational methods

We have computed pathways for methane sequential decomposition on $Fe_3Ni(111)$ and Ni(111) surfaces within the framework of spin-polarized density functional theory, using the Vienna Ab Initio Simulation Package (VASP) [40–43] using the generalized gradient approximation of Perdew, Burke, and Ernzerhof to represent the exchange-correlation energy [44] and Projector Augmented Wave (PAW) pseudopotentials (400 eV energy cutoff) to represent electron–ion-core interactions [45,46]. Electron occupancies were determined according to the Fermi scheme with 0.1 eV energy smearing. Monkhorst-Pack (9 × 9 × 9) and (3 × 3 × 1) k-point meshes were used to sample the bulk and surface Brillouin zones, respectively [47]. Self-consistent field calculations were converged to 1.0×10^{-5} eV/atom and geometries were optimized using a force convergence of 0.02 eV/Å. The transition state (TS) structures and the reaction pathways were located using the climbing image nudged elastic band (CI-NEB) method [48] with a 0.02 eV/Å force tolerance. Harmonic vibration frequency calculations were carried out for all the transition states of CH_x (x = 0–4) on $Fe_3Ni(111)$.

2.5. Computational models

The optimized bulk structures of fcc-Fe_3Ni and fcc-Ni obtained through the Birch–Murnaghan equation of state matched well with experimental data [49]. The optimized lattice constants were 3.591 Å and 3.517 Å for fcc-Fe_3Ni and fcc-Ni, respectively (exp. 3.575 Å and 3.524 Å, respectively), corresponding to fractional errors of 0.1 % and 0.2 %, respectively [50,51]. The good agreement with experiments indicates that this approach is appropriate for modeling these systems. $Fe_3Ni(111)$ and Ni(111) surfaces were modelled as three-layer slabs, where the bottom layer was fixed using a (2 × 2) supercell and a 20 Å vacuum region.

The adsorption energy, E_{ads}, was calculated as follows:

$$E_{ads} = E_{adsorbates/slab} - (E_{adsorbates} + E_{slab}) \quad (7)$$

where $E_{adsorbates/slab}$, $E_{adsorbates}$, E_{slab} represent the total energy of adsorbed species (and the slab), isolated adsorbate species, and the isolated slab (i.e., $Fe_3Ni(111)$ or Ni(111)), respectively, where isolated adsorbate energies were calculated by putting one molecular adsorbate in a 10 × 10 × 10 Å cubic cell.

The reaction energy of each step in CH_4 decomposition, E_{react}, was calculated in the way of:

$$E_{react} = E_{CH_{x-1}/H/slab} - E_{CH_x/slab} \quad (8)$$

where $E_{CH_{x-1}/H/slab}$ is the total energy of adsorbates CH_{x-1} and H on the surface and $E_{CH_x/slab}$ is the total energy of CH_x adsorption on the surface.

The split energy, E_{split}, defined as the energy required to separate CH_{x-1} and H far enough on the surface to eliminate interactions was calculated by:

$$E_{split} = E_{CH_{x-1}/slab} + E_{H/slab} - (E_{CH_{x-1}/H/slab} + E_{slab}) \quad (9)$$

where $E_{CH_{x-1}/slab}$ and $E_{H/slab}$ are the total energies of adsorbates CH_{x-1} and H adsorption on the surface, respectively. Negative values mean that separation of CH_{x-1} and H is exothermic after CH_x decomposition on the surface, while the positive values indicate that CH_{x-1} and H energetically prefer to remain close to each.

3. Results

3.1. Methane decomposition

Characterizations including XRD, H_2-TPR, and Raman tests were conducted for screening COCs (CF, CFA, CFC, CFN, CFAC, and CFAN) as shown in Figs. S1-S3. Elemental compositions, textural properties, and crystallite sizes of as-prepared and reacted samples are provided in the Supplementary Material (See Tables S2-S4). Thermogravemetric experiments were conducted for the COCs screening as shown in Fig. 1, in which Fig. 1A-D indicates the results of a typical CLMDCR cycle, the mass evolution of CH_4 decomposition stage, the mass changes during CO_2 reduction stage, and the CO_2 temperature programmed oxidation (CO_2-TPO) experiments carried out by TGA, respectively. Results indicate that the CFAN shows the best performances among the six tested COCs from both methane decomposition and CO_2 reduction activities. After comprehensively consideration of the TG results from Fig. 1A-C, the catalytic performances of the COCs follows the order of CFAN > CFAC > CFA > CFN > CFC while CF shows negligible reactivity. Moreover, the CO_2-TPO experiments show the CO_2 reduction reactivity of carbon deposited CFAN sample is superior than the other COCs, as seen in Fig. 1D. Thus, CFAN was chosen for further investigation

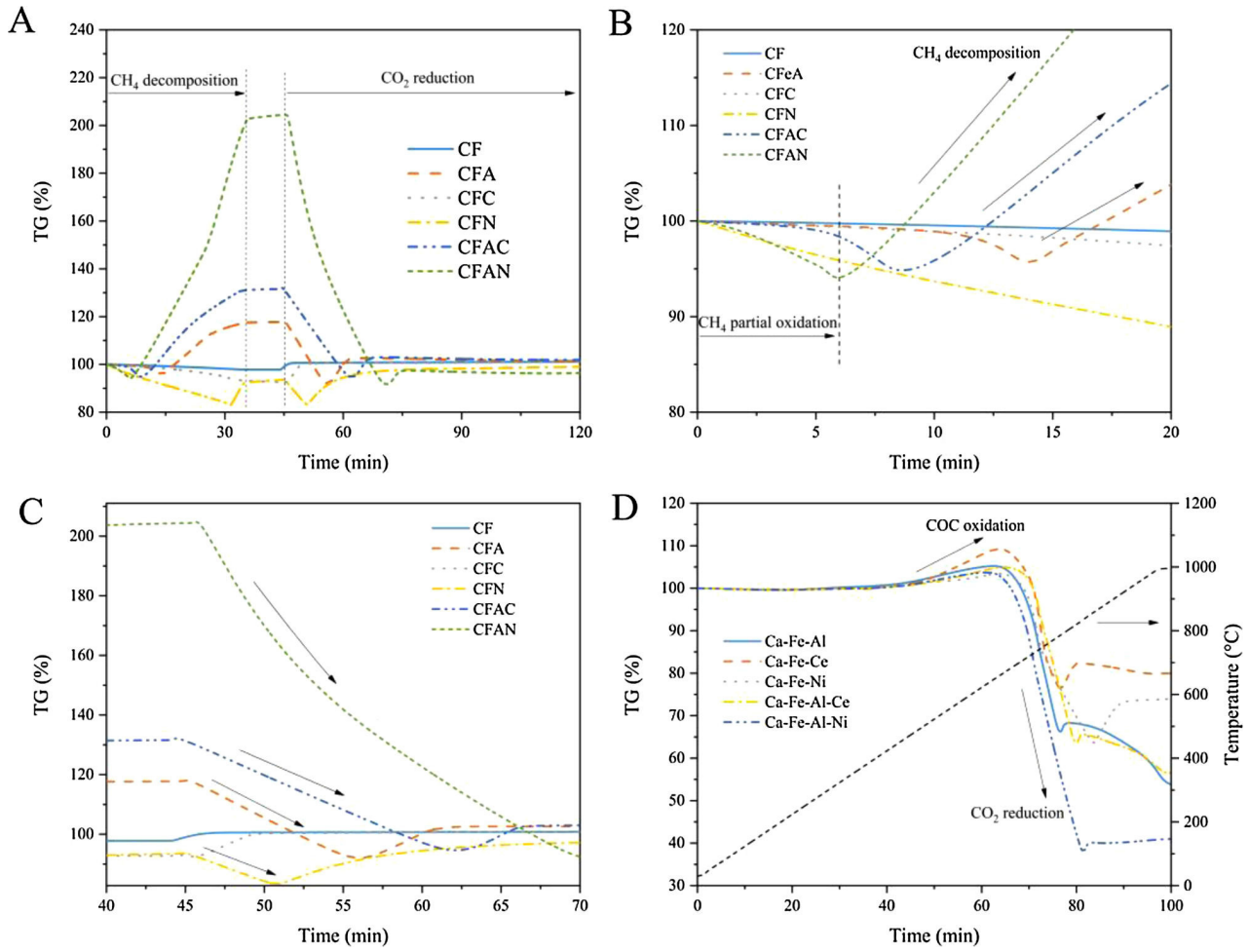

Fig. 1. TG experiments for COCs screening. Evolution of sample weight (%) as a function of time: A) CH_4 decomposition at 750 °C with CO_2 reduction at 800 °C; B) CH_4 decomposition at 750 °C; C) CO_2 reduction at 800 °C; D) CO_2 temperature programmed oxidation (CO_2-TPO) with applied TGA from room temperature to 1000 °C with a heating rate of 10 °C/min and CO_2 concentration of 20 vol.% in N_2 using 1 h reacted COCs.

including its redox activity, cyclic durability, forms and amount of deposited nano-carbon material, phase and morphology evolution.

TEM, STEM, and TEM-EDX mappings were carried out to investigate the morphology and distribution of Ni in the as-prepared CFAN sample (See Fig. 2). The particles with a spacing of 0.731 nm corresponded to the $Ca_2Fe_{1.52}Al_{0.48}O_5$(020) facet (JCPDS 71 − 0667). Additionally, the morphology of the $Ca_2Fe_{1.52}Al_{0.48}O_5$ support was considered to be as closely packed hexagons based on TEM and the STEM images. The EDX mapping results revealed that the particle size of $NiFe_2O_4$ (JCPDS 86–2267) was small and was homogeneously dispersed on the surface of $Ca_2Fe_{1.52}Al_{0.48}O_5$.

The TEM images of 0.5 h reacted CFAN sample are displayed in Fig. S4a and Fig. S4b. The morphology of produced nano-carbon, carbon nanotubes (CNTs), were observed. The particles with a d-spacing of 0.207 nm were assigned to be Ni-Fe alloy (JCPDS 47–1417) with (111) facet exposed and the d-spacing of 0.279 nm was attributed to $Ca_2Fe_{1.4}Al_{0.6}O_5$(200) (JCPDS 70–1498), resulting from trace reduction of $Ca_2Fe_{1.52}Al_{0.48}O_5$ (Fig. S4c). Further, the detection of CaO (JCPDS 99 − 0070) from 0.5 h reacted CFAN sample is proof of the reduction of $Ca_2Fe_{1.52}Al_{0.48}O_5$. Raman spectra were also recorded to understand the degree of graphitization of the deposited nano-carbon found in the CFAN sample reacted for 1 h as shown in Fig. S4d. Three main peaks at 1345 cm^{-1}, 1575 cm^{-1}, and 2675 cm^{-1} were observed in the spectra, which were ascribed to D, G, and G' bands, respectively. It is reported that the D band represents disordered aromatic structures, while the G band denotes the condensed, ordered, or graphitic aromatic structures [52–54]. Thus, the ratio of G band to D band intensity (I_G/I_D) represents the degree of graphitization, which reflects the ease of carbon oxidation by CO_2 [53]. The graphitic degree of the deposited carbon follows the order of CFAN < CFAC < CFC < CFA < CFN, as displayed in Table S5, indicating that the deposited carbon from CFAN has the highest activity toward CO_2 oxidation.

To understand the morphology of the 1 h reacted CFAN and CNTs resulting from one side of CLMDCR, TEM analysis was conducted, and the images are shown in Fig. 3A and Fig. 3B. The dark spots indicate the presence of Ni-Fe particles and the irregular bulk in Fig. 3A is assumed to be the CFAN support that holds the Ni-Fe alloy. It is observed that the diameter of the CNTs varies from 10 to 20 nm. The well distribution of Ca, Fe, Al and O elements on the 1 h reacted CFAN are demonstrated in Fig. 3F. Moreover, the EDX mapping results reveal that the observed carbon exists in a form of carbon nanotube and Ni exists as small particles which disperses on the $Ca_2Fe_xAl_{2-x}O_5$ support.

Fig. 3C shows the XRD patterns of 0.5 h reacted and 1 h reacted CFAN samples. The peak located near 26° was assigned to diffraction of the CNTs [25]. Three diffraction peaks at 2θ = 43.5°, 50.7°, and 74.5° were observed from both 0.5 h reacted CFAN and 1 h reacted CFAN, which are attributed to (111), (200), and (220) facets of Ni-Fe alloy (JCPDS 47–1417). Notably, the peak intensity of $Ca_2Fe_{1.52}Al_{0.48}O_5$ decreases slightly with time whereas that of CaO increases, indicating the gradual reduction of $Ca_2Fe_xAl_{2-x}O_5$. SEM and EDS mapping images of 1 h CMD reacted CFAN were displayed in Fig. S5, which also reveals the production of CNTs from Ni-Fe alloy catalyzed methane

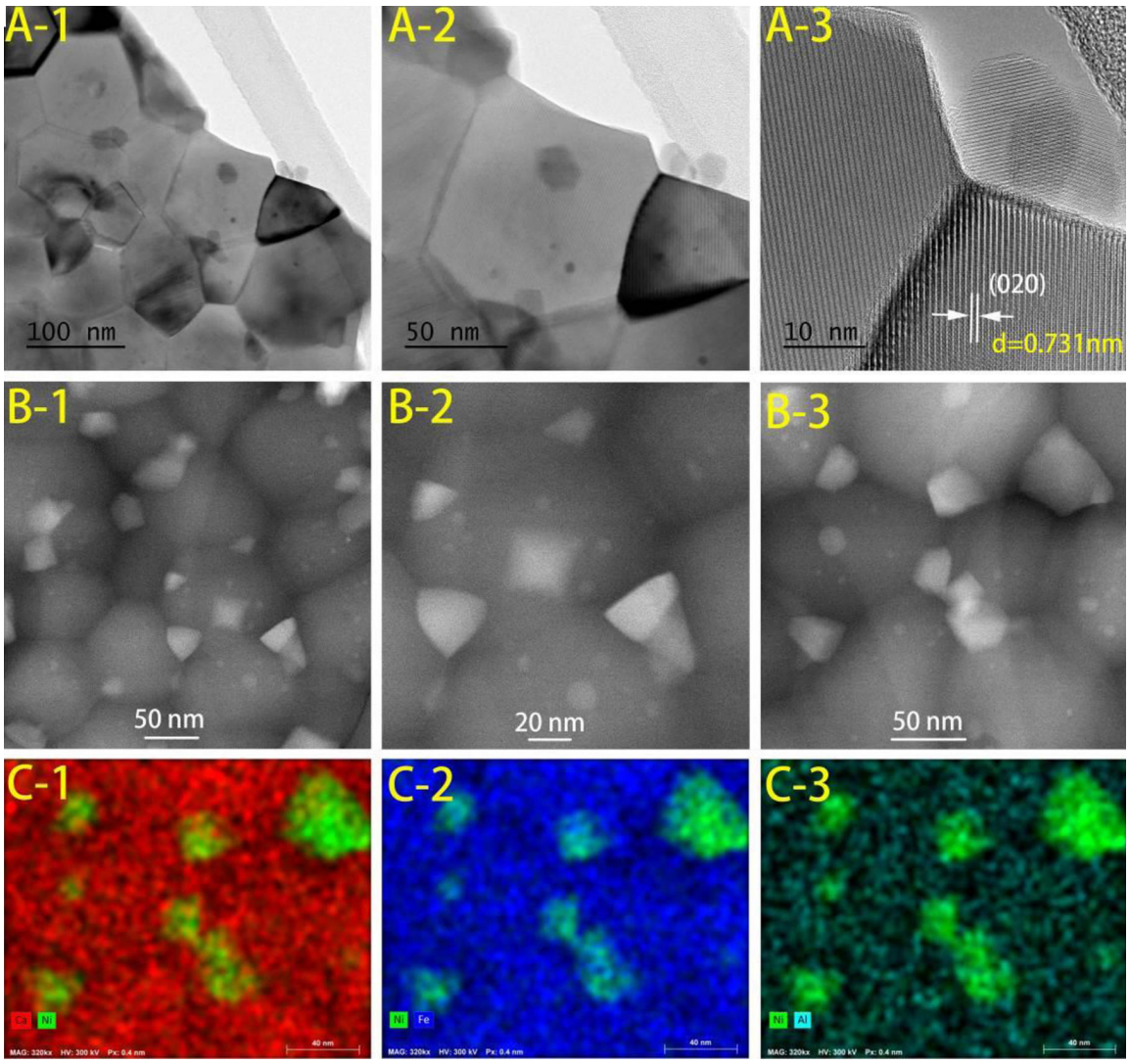

Fig. 2. Characterizations of fresh CFAN. (A) TEM; (B) STEM; and (C) TEM-EDX mapping images of the as-prepared CFAN.

decomposition.

XPS measurements were carried out to analyze the chemical state of CFAN after different CMD reaction times as presented in Fig. 3D and E. Fig. 3D shows a high-resolution spectrum of O_{1s} while Fig. 3E shows a high-resolution C_{1s} spectrum. XPS O_{1s} peaks are fitted with three sub-peaks and labeled as OI (530.4 eV), OII (532.1 eV), and OIII (533 eV), which can be ascribed to lattice oxygen (OI), surface adsorbed oxygen (OII), and hydroxyl and/or carbonate species, respectively [55]. The oxygen defect concentration is generally proportional to the OII/OI molar ratio. It is observed that the OII/OI ratio decreases significantly with CMD reaction time, which may attribute to the gradual reduction of $Ca_2Fe_{1.52}Al_{0.48}O_5$ to $Ca_2Fe_{1.4}Al_{0.6}O_5$, CaO, and Fe generation. The generation of CaO and Fe results in the decrease of oxygen defect concentration (See Table 1). Moreover, the intensity of the peak at 284.8 eV, attributed to sp2 hybridized C, strongly increases (carbon atomic percent from 65.6%–93.7%) with the increase in CH_4 decomposition within 0.5 − 1 h, indicating the accumulative deposition of carbon with time (See Fig. S6).

Experimental results indicate that the temperatures within 750 − 800 °C are optimal for CLMDCR including methane decomposition and CO_2 to CO conversion. Higher temperatures (> 800 °C) will lead to the deactivation of COC while the temperatures lower than 750 °C are not conductive to C–H bond activation which performs slow decomposition kinetics. The methane decomposition and carbon dioxide reduction results are presented in Fig. 4 (See Figs. S7-S9). Fig. 4A and B show the methane conversion and hydrogen concentration during the CMD stage. It is observed that both CH_4 conversion and H_2 concentration can be maintained higher than 90 % between 750 − 800 °C. The hydrogen yield could reach approximately 240 $mmolH_2\ h^{-1}\ g^{-1}$·COC. For CO_2 reduction stage, the CO production rate initially increases rapidly during CO_2 reduction and then stabilizes (Fig. 4C). After the CO yield stabilized for a period of time (~ 40 min), it decreases gradually due to the decreasing amount of the deposited carbon. Results from Fig. S9 indicate that the generated CO from CO_2 reduction can reach a concentration as high as 95 vol.% at 800 °C, which is a relatively low temperature compared with those used in conventional char gasification [56,57]. Further, it can be seen that the CO_2 conversion maintains at a relatively high level (> 90 %) for the first 40 min of CO_2 reduction stage; while the CO_2 conversion decreases gradually after 40 min (See Fig. 4D). Moreover, it takes longer for complete oxidation of the deposited carbon with the decrease of CO_2 reduction temperature due to the low carbon conversion rate at low temperatures. Thus, 800 °C is seen as optimal temperature for CO_2 reduction.

3.2. Cyclic stability

Multiple cycles of methane decomposition with CO_2 reduction

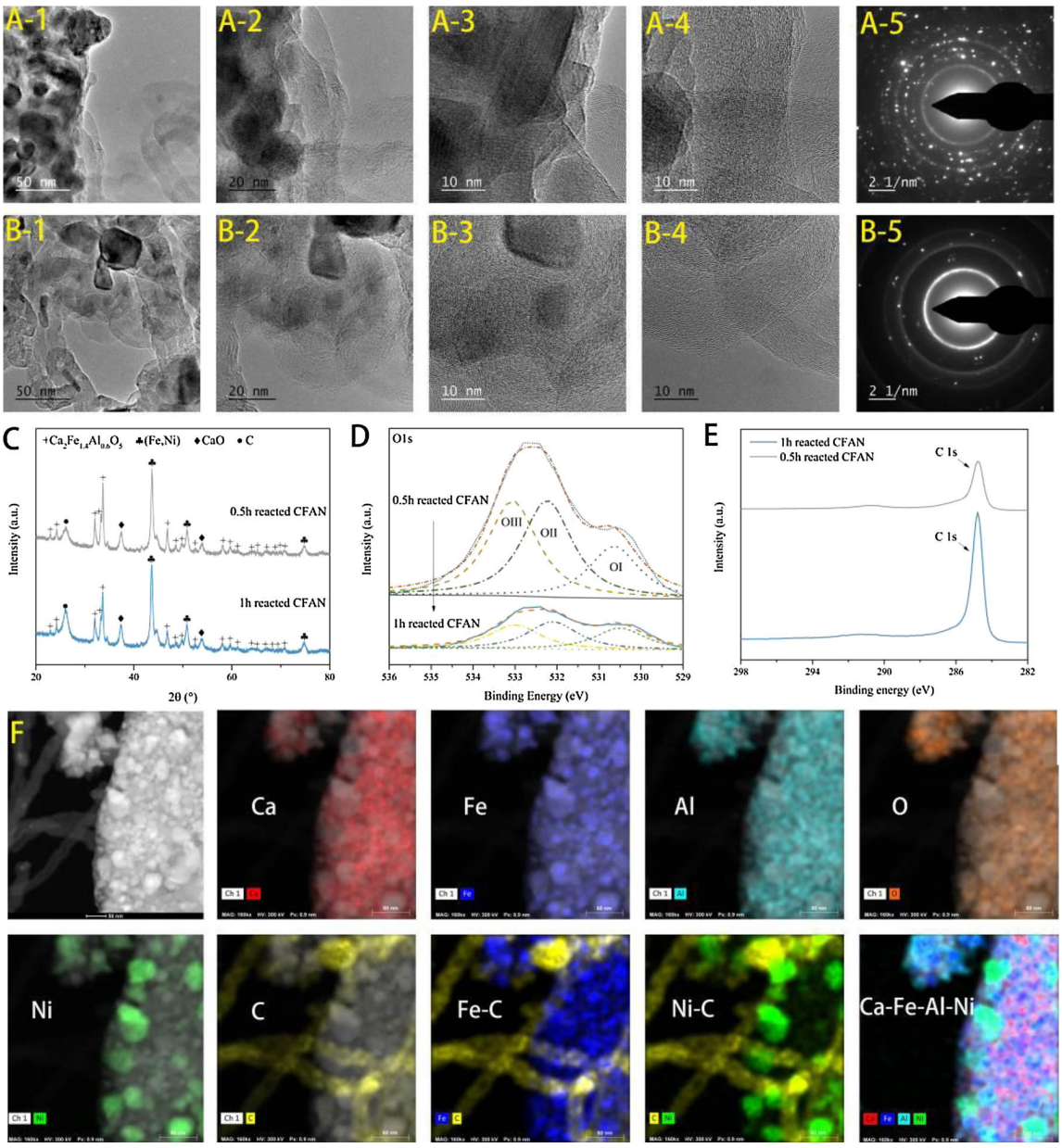

Fig. 3. Characterizations of 1h reacted CFAN: A), B) TEM images of reacted CFAN or morphology of generated CNTs after 1h CMD; C) XRD patterns; D) high-resolution XPS results of O 1s peaks; E) high-resolution XPS results of C 1s peaks; and F) TEM-EDX mapping results of 1h reacted CFAN.

Table 1
XPS-derived characteristics for 0.5 h and 1 h reacted CFAN samples.

Oxygen Carriers	Oxygen species percentages (%)			OII/OI ratios
	OI	OII	OIII	
0.5 h reacted CFAN	16.2	40.0	43.8	2.48
1 h reacted CFAN	28.8	27.2	44.0	0.95

experiments were carried out to investigate the redox stability of CFAN as displayed in Fig. 5. Based on the above experimental results, 800 °C was used for cyclic CLMDCR. It should be noted that the H_2 production rate and CO production rate of CFAC show a gradual decreasing trend after the 5th redox cycle. Moreover, CFAC shows barely catalytic activity for methane decomposition after 13 redox cycles, resulting in minimal CO generation during the CO_2 reduction stage. In contrast, the activity of CFAN remains basically unchanged after 20 cycles of CMD and CO_2 reduction stage up to 3000 min. It has been reported that the performance of CMD is highly dependent on the crystallite size of the catalyst, thus catalyst sintering and agglomeration show a major impact on CMD performance [20]. The phases of CFAC are mainly composed of CeO_2 (JCPDS 43–1002) and $Ca_2Fe_{1.52}Al_{0.48}O_5$. The existence of $Ca_2Fe_{1.52}Al_{0.48}O_5$ to some extent promotes the CeO_2 dispersion but the physical interaction shows limited influence after several redox cycles. Results from Fig. 5B and D suggest that CFAN's cyclic stability is due to the suppression of sintering and agglomeration of the Ni-Fe alloy because of the redox phase change of $Ni_yFe_{3-y}O_4$ ↔ Ni-Fe alloy and $Ca_2Fe_{1.52}Al_{0.48}O_5$ ↔ CaO + Fe + $Ca_2Fe_xAl_{2-x}O_5$ (See Table 2) [57,58]. Results from Fig. S10 also indicate the decrease of lattice oxygen mobility from both CFAC and CFAN samples with number of cycles, whcih could be attributed to the incomplete conversion of the deposited carbon as proved by the O_2-TPO experiment provided in Fig. S11. Moreover, the amount of unconverted carbon increases and the types of deposited carbon become much more complicated with the number of cycles.

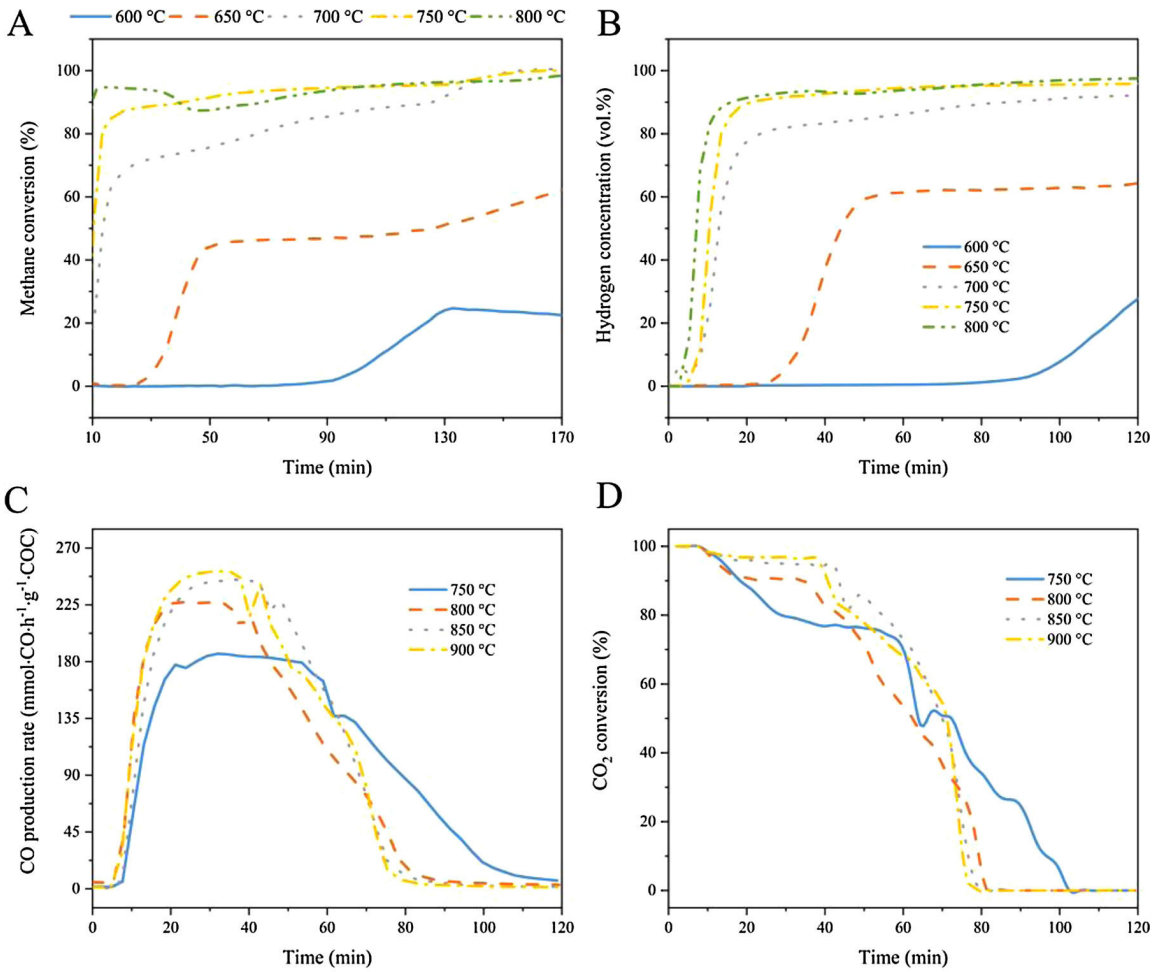

Fig. 4. Effect of temperatures on the performance of CLMDCR: A) methane conversion during CH_4 decomposition stage; B) hydrogen concentration during CH_4 decomposition stage; C) CO production rate during CO_2 reduction stage; D) CO_2 conversion during CO_2 reduction. CFAN is used as the COC, 20 vol.% CH_4 in N_2 during CH_4 decomposition stage and 20 vol.% CO_2 in N_2 during CO_2 reduction stage.

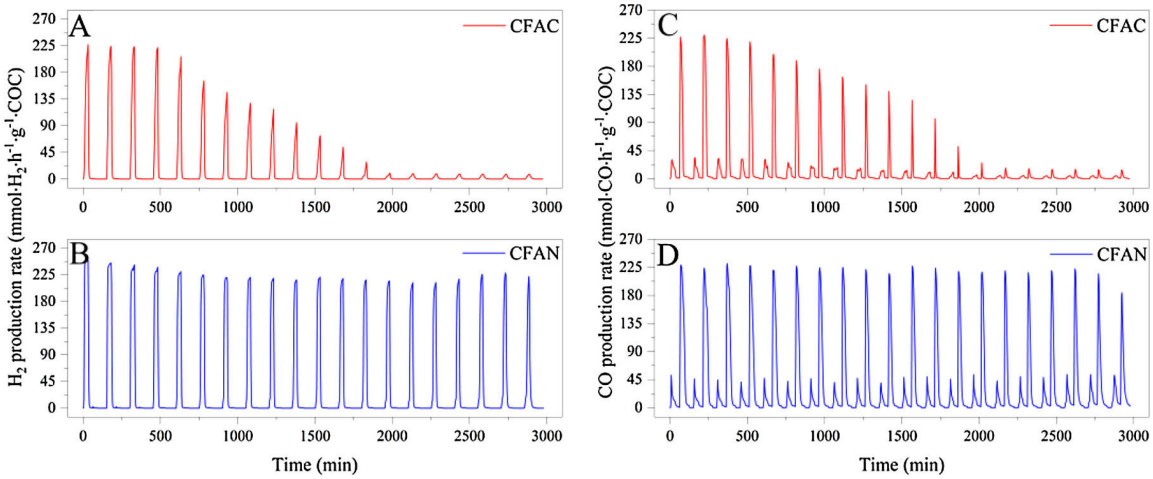

Fig. 5. Comparison of the cyclic stability of CFAC and CFAN at 800 °C: A) H_2 production rate using CFAC; B) H_2 production rate using CFAN; C) CO production rate using CFAC; D) CO production rate using CFAN.

The carbon balance during CLMDCR is calculated taking the 6th cycle as an example (See Fig. 6 and Fig. S12). As for the methane decomposition stage, the amount of deposited carbon is calculated according to the carbon balance: $Y_1(CH_4, converted) = Y_1(CO) + Y_1(CO_2) + Y_1(C)$, where $Y_1(CH_4, converted)$, $Y_1(CO)$, $Y_1(CO_2)$, and $Y_1(C)$ represent the converted CH_4, as well as the geranted CO, CO_2, and deposited carbon during the methane decomposition stage. The integration results of $Y_1(CH_4, converted)$, $Y_1(CO)$, and $Y_1(CO_2)$ are 48.23 mmol·CH_4 h^{-1} g^{-1}·COC, 10.82 mmol·CO h^{-1} g^{-1}·COC, and 0.81 mmol·CO_2 h^{-1} g^{-1}·COC, respectively. Thus, the resulting M(deposited carbon) is 36.60 mmol·C h^{-1} g^{-1}·COC. As for the CO_2 reduction stage, the CO production yield was originated from the reduction of

Table 2
Crystallite size of the cycled CFAN samples.

Oxygen carriers	Crystallite size (nm)[a]		
	Support	Fe/Ni alloy	Ni
Fresh CFAN	37.8	25.4	–
1st cycled CFAN	30.8	42.9	35.7
20th cycled CFAN	28.0	58.1	60.9

[a] Calculated by Scherrer equation.

CO_2 by COC and deposited carbon. Thus, contributions of CO from reduced COC and deposited carbon were quantatively calculated. According to the integration results, the total CO production yields at the CO_2 reduction stage is 85.90 mmol·CO h^{-1} g^{-1}·COC; The small amount of unreacted carbon during CO2 reduction is neglected to simplify the calculation and thus the CO yields from deposited carbon is 73.20 mmol·CO h^{-1} g^{-1}·COC (accounts for 85.2 wt.%) because each mole of deposited carbon could produce 2 mol of CO. The CO yields originated from reduced COC is 85.90 − 73.20 = 12.70 mmol·CO h^{-1} g^{-1}·COC, accounting 14.8 wt.% of the produced CO.

XRD, H_2-TPR, N_2 adsorption and desorption isotherms, as well as TEM-EDX mapping were performed to analyze the physical and chemical properties of the CFAN after 20 cycles (Fig. 7). From Fig. 7A, it is seen that 1) $Ca_2Fe_{1.52}Al_{0.48}O_5$ and $Ni_{0.4}Fe_{2.6}O_4$ are redox stable components after 20 cycles of CLMDCR; 2) Ni° is observed in both 1st cycled and 20th cycled CFAN samples, which indicates that nickel exists as Ni° in addition to $Ni_{0.4}Fe_{2.6}O_4$; 3) sintering and agglomeration partially occurs on the cycled CFAN, causing the particle size to increase temporally, while the cycled CFAN maintains its fine dispersion on the support which could be attributed to the redox looping of $Ni_{0.4}Fe_{2.6}O_4$↔Ni-Fe alloy.

The H_2 reduction behaviors of as-prepared, 1st cycled, and 20th cycled CFAN were examined by H_2-TPR (See Fig. 7B). As noted, three H_2 consumption peaks appear in H_2-TPR at 414 °C, 573 °C, and 900 − 915 °C for fresh CFAN. The shoulder peak and the second peak were attributed to the reduction of $NiFe_2O_4$ and the third peak arose from the reduction of the $Ca_2Fe_xAl_{2-x}O_5$ support. Three peaks at 309 °C, 565 °C, and 929 °C were observed for CFAN after the first cycle and peaks located at 290 °C, 558 °C, and 939 °C were seen after 20 cycles. The first two peaks of cycled CFAN shift to a lower temperature range due to the phase transformation from $NiFe_2O_4$ to $Ni_{0.4}Fe_{2.6}O_4$ while the third peak shifts to a slightly higher temperature range. The high-temperature reduction peak did not significantly shift for the cycled CFAN samples, indicating a relatively stable $Ca_2Fe_xAl_{2-x}O_5$. Moreover, the required temperature of $Ni_{0.4}Fe_{2.6}O_4$ reduction decreases with the number of cycles, ensuring the complete reduction of $Ni_{0.4}Fe_{2.6}O_4$ to Ni° and the formation of Ni-Fe alloy.

The evolution of BET surface areas from fresh CFAN, after 1 and 20 cycles of CLMDCR was compared to that of CFAC (Table 3). As can be seen in Fig. 7C, both BET surface areas of CFAN and CFAC show a tendency of decreasing after 1 redox cycle, which decreases by 25.4 % and 12.7 %, respectively. The phenomenon could be attributed to the instability of the as-prepared CFAN sample such as its phases evolution during the first cycle of CLMDCR. However, both the BET surface areas of CFAC (122.4–112.1 m^2/g) and CFAN (121.3–113.1 m^2/g) stabilize and only a slight decrease can be observed from the 1st to 20th redox cycle. The possible reasons can be explained as: 1) After 1st redox looping, the phase of CFAN evolves and forms a stable phase ($NiFe_2O_4$→$Ni_{0.4}Fe_{2.6}O_4$), therefore remaining relatively stable BET surface area; 2) The sintering as well as the agglomeration of COC could

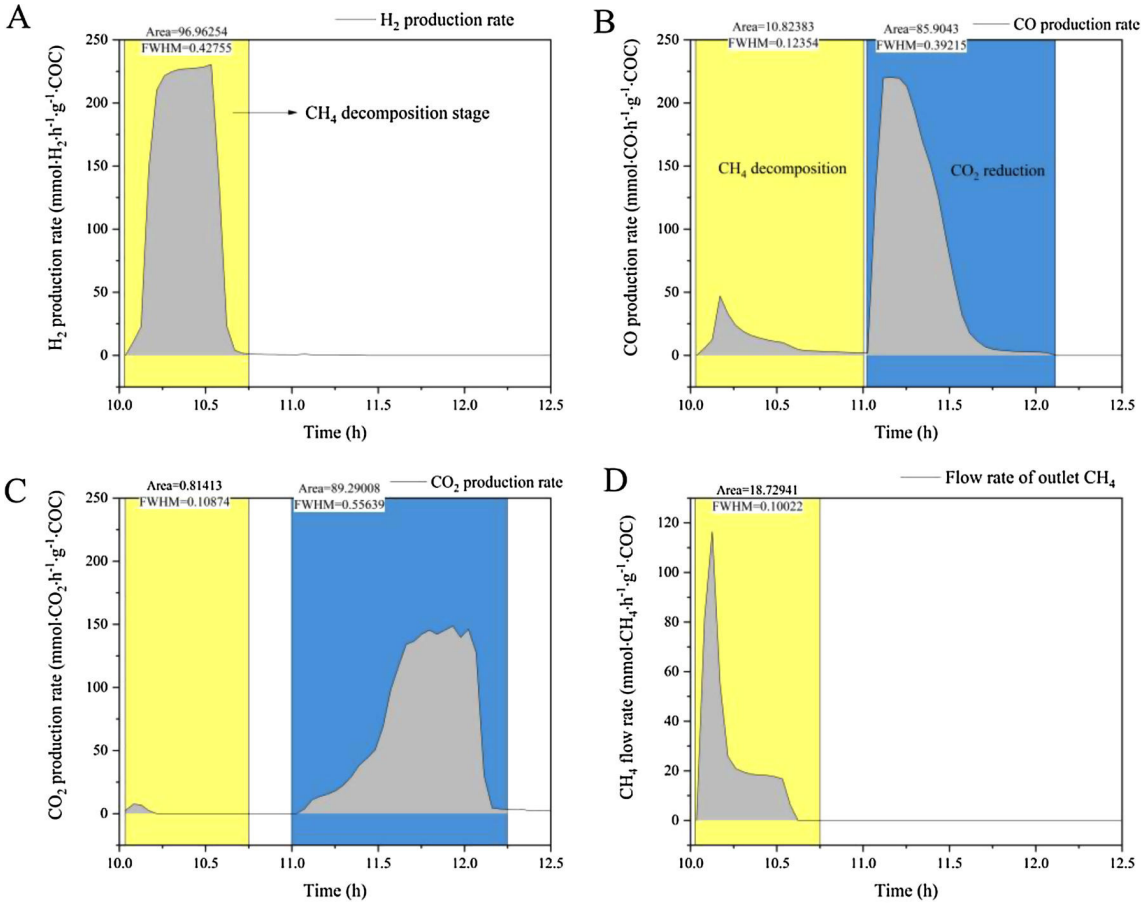

Fig. 6. Carbon balance calculation of the 6th CLMDCR cycle: A) H_2 yields; B) CO yields; C) CO_2 yields; and D) CH_4 yields.

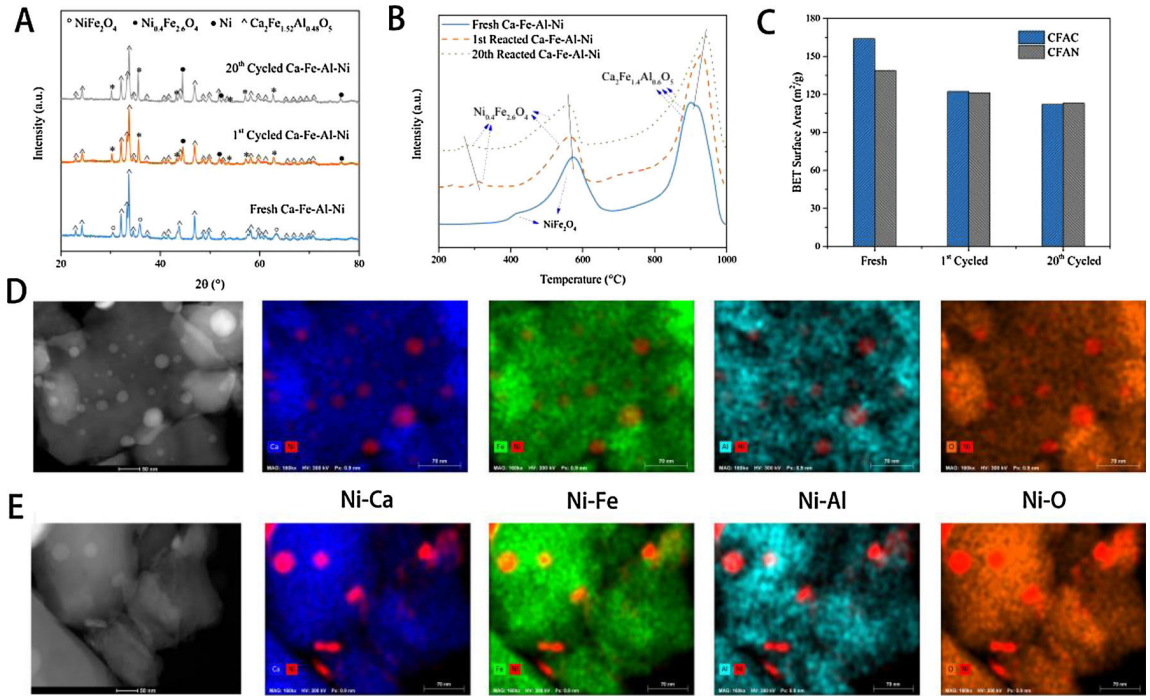

Fig. 7. Characterization of 1 st and 20th cycled CFAN: A) XRD patterns; B) H_2-TPR profiles; C) BET surface area distributions; D) TEM-EDX mapping results of 1st cycled CFAN; and E) TEM-EDX mapping results of 20th cycled CFAN.

Table 3
Textural properties of the as-prepared and cycled catalysts.

Oxygen carriers	Average pore diameter (nm)	BET surface area (m^2/g)	Pore volume (g/cm^3)
Fresh CFAC	4.0	164.0	0.157
Fresh CFAN	5.1	138.9	0.169
1st cycled CFAC	4.0	122.4	0.117
1st cycled CFAN	4.3	121.3	0.113
20th cycled CFAC	4.0	112.1	0.097
20th cycled CFAN	3.8	113.1	0.104

be suppressed because they were homogenized into $Ni_yFe_{3-y}O_4$-$Ca_2Fe_xAl_{2-x}O_5$ on an atomic level in the CO_2 reduction stage; 3) Nevertheless, the BET surface areas of CFAC and CFAN samples still perform slight decreasing tendency which maybe attributed to the carbon deposition.

The dispersion of cycled $Ni_{0.4}Fe_{2.6}O_4$ and/or Ni on $Ca_2Fe_{1.52}Al_{0.48}O_5$ was confirmed using TEM and EDX mapping of CFAN samples (Figs. 7D, E, and Fig. S13). The particle sizes of 1st cycled $Ni_{0.4}Fe_{2.6}O_4$ and/or Ni were well dispersed on the $Ca_2Fe_xAl_{2-x}O_5$ support and remain dispersed beyond 20 cycles. The Ni-containing particle sizes of 20th cycled CFAN have increased due to sintering and agglomeration, but still remains relatively small particle sizes, which was in agreement with the XRD results.

3.3. DFT calculation

Experimental results indicate that catalytic activity of methane decomposition to form high purity hydrogen is due to the presence of the Ni-Fe alloy, and not pure Ni. Additionally, the stability of the deposited carbon species on the COC surface is crucial to generating nano-carbon, and thus for CO production. For these reasons, DFT simulations on the sequential decomposition of methane on $Fe_3Ni(111)$ were carried out. A Fe/Ni ratio of 3 (the details of the ratio is discussed in Supplementary Material) is adopted as a representative composition. Similar CMD behavior on Ni(111) was investigated for comparison.

3.3.1. Adsorption of CH_x (x = 0–4) and H on $Fe_3Ni(111)$

CH_x intermediates on Ni and bimetallic alloys have been shown to adsorb to threefold sites [59,60]. In our calculations, six typical adsorption sites for CH_x (x = 0–4) and H on $Fe_3Ni(111)$ surface were investigated, including Top (T_{Fe} and T_{Ni}), Hollow (H_{3Fe} and H_{FeNi}) and Bridge sites (B_{FeFe} B_{FeNi}), as shown in Fig. S14. The most energetically favorable site for CH_x and H on $Fe_3Ni(111)$ was shown to be the Hollow site; however, H_{3Fe} and H_{FeNi} sites show a comparable affinity (See Fig. 8A). Therefore, both H_{3Fe} and H_{FeNi} sites were further studied. Calculated adsorption energies suggest that CH_x (x = 0–3) can chemically adsorb on $Fe_3Ni(111)$ and Ni(111) surfaces and the adsorption energy is proportional to the extent of dehydrogenation. Moreover, the more negative values of adsorption energies indicate CH_x (x = 0–3) and H can bind more strongly with a Ni-Fe alloy surface than pure nickel. In particular, the adsorption of C on $Fe_3Ni(111)$ surfaces was 0.59 eV larger than that on Ni(111) surfaces, indicating carbon is more stable on $Fe_3Ni(111)$ surfaces. Detailed information about the adsorption energies and geometries are provided in the Supplementary Material (See Fig. S15 and Fig. S16).

3.3.2. Methane decomposition on Fe3Ni(111)

To reveal the mechanism of sequential methane decomposition on $Fe_3Ni(111)$, consisting of four steps (Steps 1–4), the co-adsorption of CH_x (x = 0–3) on H_{3Fe} /H_{FeNi} sites and H on opposite or interval threefold sites (Fig. 8B) were investigated. The reaction energies of each step are plotted in Fig. 8C. The details of co-adsorption modes, including linear (Sites 1, 3, and 5) and zigzag (Sites 2, 4, and 6) modes, are given in Fig. S17. The most thermodynamically favorable pathway (p1) involves CH_x adsorption on H_{3Fe} sites, while H adsorbs opposite CH_x. By contrast, CH_x adsorption on H_{FeNi} corresponds to H adsorption on interval sites (p2). In summary, these two pathways for stepwise decomposition of methane can be described based on the adsorption site of H in each step as:

$$CH_4 \xrightarrow{\text{Site 1}} CH_3 + H \xrightarrow{\text{Site 1}} CH_2 + 2H \xrightarrow{\text{Site 1}} CH + 3H \xrightarrow{\text{Site 1}} C + 4H \quad \text{(p1)}$$

$$CH_4 \xrightarrow{\text{Site 6}} CH_3 + H \xrightarrow{\text{Site 4}} CH_2 + 2H \xrightarrow{\text{Site 6}} CH + 3H \xrightarrow{\text{Site 5}} C + 4H \quad \text{(p2)}$$

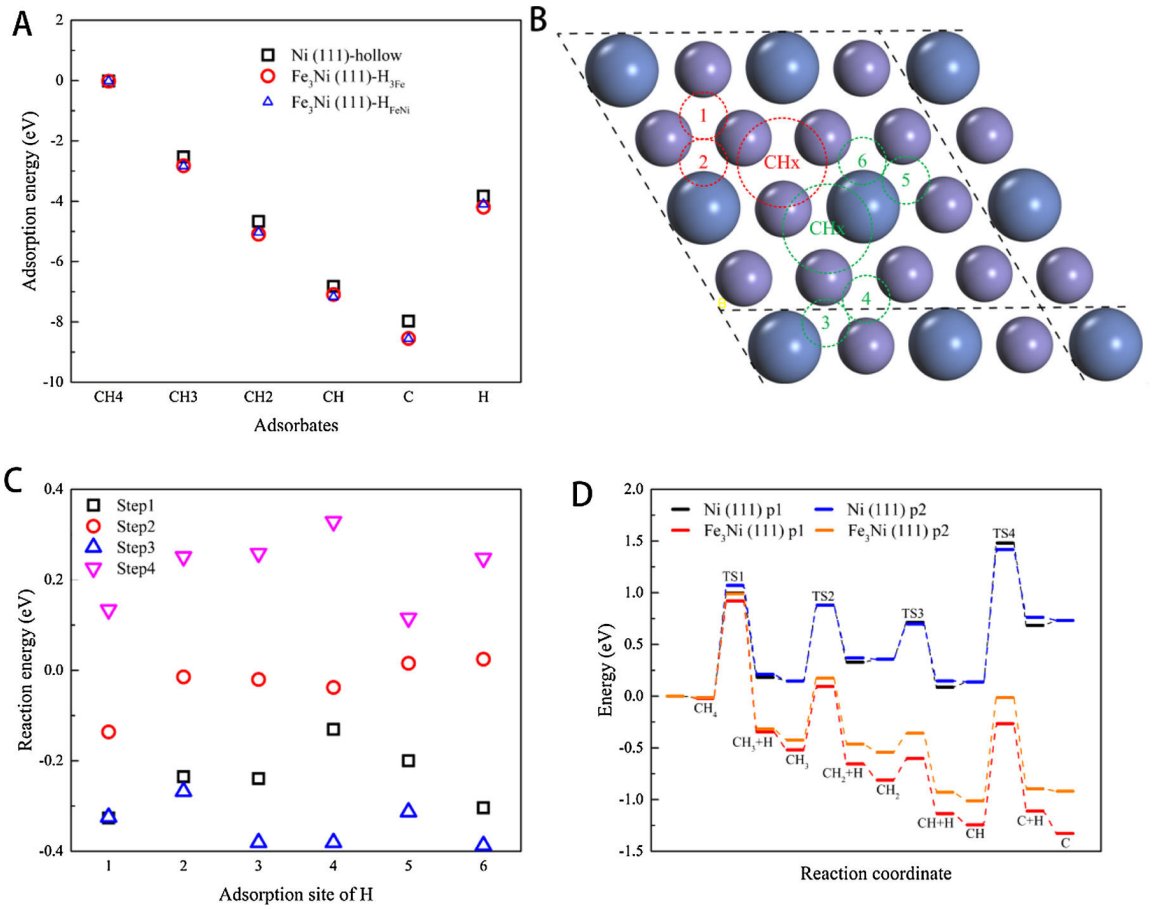

Fig. 8. DFT calculations. (A) Adsorption energies of single CH_x (x = 0-4) or H on $Fe_3Ni(111)$ H_3Fe site (red circle), HFeNi site (blue triangle) and Ni(111) hollow site (black square); (B) six co-adsorption sites of CH_x (x = 0-3) and H on $Fe_3Ni(111)$. Only the top layer is shown for clarity. Blue and purple balls are Ni and Fe atoms, respectively; (C) reaction energies of each step occurring on different sites. Step 1 (black squares), Step2 (red circles), Step 3 (blue up triangles) Step 4 (pink down triangles); and (D) potential energy diagram of CH_4 decomposition on $Fe_3Ni(111)$ and Ni(111).

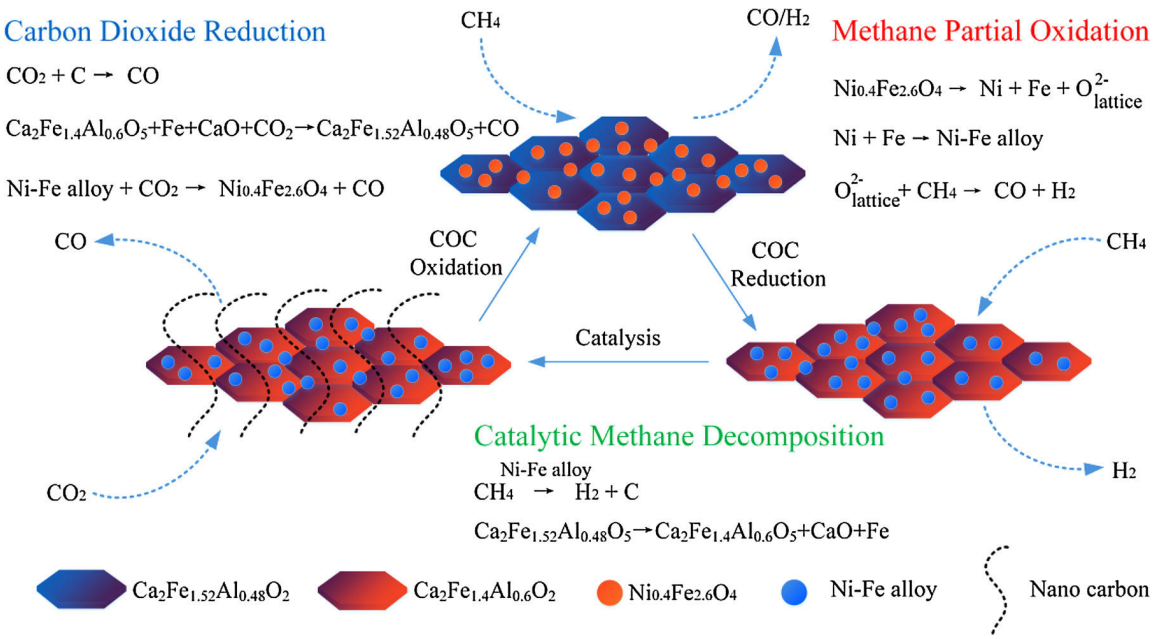

Fig. 9. Catalytic mechanisms during the redox cycle of CMDCR. The COC promotes methane partial oxidation (COC reduction), catalytic methane decomposition (catalysis), and carbon dioxide reduction (COC re-oxidation), respectively.

To better illustrate the superiority of the Ni-Fe alloy, the potential energy diagram of CH_4 decomposition on $Fe_3Ni(111)$ is shown alongside two similar pathways on Ni(111) in Fig. 8D and the detailed energy information are listed in Table S6. For pure Ni(111), the overall reaction of CH_4 decomposition is endothermic. The third step, $CH_2 \rightarrow CH + H$, is the only exothermic process with the lowest reaction barrier, 0.36 eV and 0.34 eV in p1 and p2, respectively. CH decomposition is the most endothermic step, with reaction energies of 0.55 eV (p1) and 0.63 eV (p2), and has the greatest forward reaction barrier, 1.34 eV and 1.28 eV in p1 and p2, respectively. Hence, the rate-limiting step of CH_4 decomposition on Ni(111) is CH decomposition. Moreover, the reaction barriers for the first step are also relatively high, estimated to be 1.01 eV (p1) and 1.09 eV (p2), respectively, which are in agreement with previous reports (1.04 eV [61], 1.09 eV [62]).

The first three steps, and the overall reaction of CH_4 decomposition on $Fe_3Ni(111)$ were found to be exothermic, indicating that continuous CH_x decomposition on $Fe_3Ni(111)$ is thermodynamically favorable. Furthermore, the reaction barriers at each step of the process on Fe_3Ni (111) decreased compared to those on Ni(111). The barrier to C–H bond breaking decreased by 0.36 eV (p1) and 0.28 eV (p2). Therefore, the CH_4 decomposition on $Fe_3Ni(111)$ was both thermodynamically and kinetically more favorable than on Ni(111).

4. Discussion

Based on the abovementioned experimental and theoretical computation results, potential reaction paths in the CLMDCR via $Ni_yFe_{3-y}O_4$-$Ca_2Fe_xAl_{2-x}O_5$ are proposed and presented in Fig. 9. The CLMDCR process can be divided into three stages: methane partial oxidation, methane decomposition, and carbon dioxide reduction. During methane partial oxidation, the lattice oxygen provided by $Ni_yFe_{3-y}O_4$ and $Ca_2Fe_{1.52}Al_{0.48}O_5$ at the initial period of chemical looping acts as the oxidizing agent, achieving a short-term methane partial oxidation. In CH_4 decomposition, hydrogen and nano-carbon materials are generated from the catalysis of Ni-Fe alloy; $Ca_2Fe_{1.52}Al_{0.48}O_5$ can be also slightly reduced by CH_4 or H_2, resulting in an increase in the Fe/Ni ratio. During CO_2 reduction, the produced nano-carbon, Ni-Fe alloy, and reduced $Ca_2Fe_{1.52}Al_{0.48}O_5$ were oxidized by CO_2 with CO production. The CLMDCR process continuously converts CH_4 to high-concentration H_2 and CO through the redox looping of $Ni_yFe_{3-y}O_4$-$Ca_2Fe_xAl_{2-x}O_5$.

$Ni_yFe_{3-y}O_4$-$Ca_2Fe_xAl_{2-x}O_5$ was designed to provide an alternative driving force to homogenize the Ni-containing catalyst at an atomic level during redox cycles through phase transformations ($Ni_yFe_{3-y}O_4 \leftrightarrow Ni + Fe$ and $Ca_2Fe_{1.52}Al_{0.48}O_5 \leftrightarrow CaO + Fe + Ca_2Fe_xAl_{2-x}O_5$, $x < 1.52$), thereby facilitating catalytic activity and redox durability at high temperatures. XRD combined with TEM-EDX mapping results indicate that the unique phase transition during redox looping makes it easier to maintain homogenous dispersion on the support with a small particle size distribution. Furthermore, $Ca_2Fe_xAl_{2-x}O_5$ not only plays a role in dispersing the active component but also takes part in the formations of Ni-Fe alloy at CMD stage (Fe^0 release) and $Ni_yFe_{3-y}O_4$ in CO_2 reduction stage (Fe^{3+} re-organization).

5. Conclusion

In this study, a highly effective and multifunctional catalytic oxygen carrier, $Ni_yFe_{3-y}O_4$-$Ca_2Fe_xAl_{2-x}O_5$, was successfully prepared and evaluated in the CLMDCR process. The CLMDCR process can be divided into three stages: methane partial oxidation, catalytic methane decomposition, and CO_2 reduction with COC regeneration. Results indicate that CFAN is a promising initiator due to the fact that 1) 96.3 vol.% H_2 is obtained through the Ni-Fe alloy catalyzed CH_4 decomposition at 750 °C; 2) CO_2 oxidation of the CFAN and deposited nano-carbon results in 95.2 vol.% CO production; and 3) significant redox durability is shown during CLMDCR. Our investigations also indicate that the nano-carbon catalyzed by CFAN performs low-degree graphitization, indicating that the deposited carbon can be oxidized by CO_2 at a relatively low temperature, which was confirmed by Raman spectroscopy.

Results from DFT calculations indicate that the CH_4 decomposition on $Fe_3Ni(111)$ is both thermodynamically and kinetically favorable compared to Ni(111). The overall reaction changed from endothermic to exothermic and the barrier in the rate-limiting step, $CH \rightarrow C + H$, decreased by 0.28 − 0.36 eV, depending on the pathways. Additionally, mechanisms for inhibiting the deactivation of CFAN at high temperatures were investigated. Sintering and agglomeration of Ni-containing particles could be suppressed due to the atomic-level homogenization via the cooperation of redox-reversible Ni and $Ca_2Fe_xAl_{2-x}O_5$ support, maintaining the particle size of CFAN even after 20 redox cycles.

The CLMDCR process provides a new implication for the efficient conversion of methane to hydrogen and CO_2 reduction to CO at relatively low temperatures. The greatest superiority of CLMDCR compared to methane dry reforming is that the high-purity hydrogen and carbon monoxide can be separately generated from CLMDCR. On one hand, the technology is expected to break through existing technologies to achieve a clean, efficient, and sustainable hydrogen energy systems; on the other hand, the CLMDCR not only ensures the negative emission of CO_2 during CLMDCR, but also achieves the CO_2 utilization, expecting to effectively solve the global warming caused by anthropogenic CO_2 emissions.

CRediT authorship contribution statement

Zhao Sun: Conceptualization, Data curation, Investigation, Formal analysis, Writing - original draft, Writing - review & editing. **Tianyi Cai:** Software, Investigation, Writing - original draft. **Christopher K. Russell:** Writing - review & editing. **J. Karl Johnson:** Methodology, Writing - review & editing. **Run-Ping Ye:** Investigation. **Wenguo Xiang:** Writing - review & editing. **Xiaoping Chen:** Writing - review & editing. **Maohong Fan:** Project administration, Resources, Supervision, Funding acquisition. **Zhiqiang Sun:** Project administration, Resources, Supervision, Funding acquisition.

Declaration of Competing Interest

The authors declare that they have no known competing financial interests or personal relationships that could have appeared to influence the work reported in this paper.

Acknowledgements

We would like to thank colleagues, collaborators, and peers for their work cited in this article. This work was supported by National Science Foundation of US (1632899) and Innovation-Driven Project of Central South University (2020CX008). Calculations were carried out at the University of Pittsburgh Center for Research Computing and using resources provided by the Extreme Science and Engineering Discovery Environment (XSEDE), which is supported by National Science Foundation grant number ACI-1548562, under allocation No. TG-DMR110091.

Appendix A. Supplementary data

Supplementary material related to this article can be found, in the online version, at doi:https://doi.org/10.1016/j.apcatb.2020.118938.

References

[1] A. Sartbaeva, V. Kuznetsov, S. Wells, P. Edwards, Hydrogen nexus in a sustainable energy future, Energy Environ. Sci. 1 (2008) 79–85.
[2] Y. Goto, T. Hisatomi, Q. Wang, T. Higashi, K. Ishikiriyama, T. Maeda, Y. Sakata, S. Okunaka, H. Tokudome, M. Katayama, S. Akiyama, H. Nishiyama, Y. Inoue, T. Takewaki, T. Setoyama, T. Minegishi, T. Takata, T. Yamada, K. Domen, A

particulate photocatalyst water-splitting panel for large-scale solar hydrogen generation, Joule 2 (2018) 509–520.
[3] Z. Sun, S. Chen, S. Ma, W. Xiang, Q. Song, Simulation of the calcium looping process (CLP) for hydrogen, carbon monoxide and acetylene poly-generation with CO_2 capture and COS reduction, Appl. Energy 169 (2016) 642–651.
[4] H. Song, X.G. Meng, Z.J. Wang, H.M. Liu, J.H. Ye, Solar-energy-Mediated methane conversion, Joule 3 (2019) 1606–1636.
[5] Z. Sun, S. Chen, C.K. Russell, J. Hu, A.H. Rony, G. Tan, A. Chen, L. Duan, J. Boman, J. Tang, Improvement of H_2-rich gas production with tar abatement from pine wood conversion over bi-functional $Ca_2Fe_2O_5$ catalyst: investigation of inner-looping redox reaction and promoting mechanisms, Appl. Energy 212 (2018) 931–943.
[6] S. Bepari, N.C. Pradhan, A.K. Dalai, Selective production of hydrogen by steam reforming of glycerol over Ni/Fly ash catalyst, Catal. Today 291 (2017) 36–46.
[7] H.F. Abbas, W.W. Daud, Thermocatalytic decomposition of methane for hydrogen production using activated carbon catalyst: regeneration and characterization studies, Int. J. Hydrogen Energy 34 (2009) 8034–8045.
[8] H.F. Abbas, W.W. Daud, Hydrogen production by methane decomposition: a review, Int. J. Hydrogen Energy 35 (2010) 1160–1190.
[9] U. Ashik, W.W. Daud, H.F. Abbas, Production of greenhouse gas free hydrogen by thermocatalytic decomposition of methane–A review, Renewable Sustainable Energy Rev. 44 (2015) 221–256.
[10] Y. Li, D. Li, G. Wang, Methane decomposition to CO_x-free hydrogen and nano-carbon material on group 8–10 base metal catalysts: a review, Catal. Today 162 (2011) 1–48.
[11] U. Ashik, W.W. Daud, Probing the differential methane decomposition behaviors of n-Ni/SiO_2, n-Fe/SiO_2 and n-Co/SiO_2 catalysts prepared by co-precipitation cum modified Stöber method, RSC Adv. 5 (2015) 67227–67241.
[12] J. Zhang, X. Li, H. Chen, M. Qi, G. Zhang, H. Hu, X. Ma, Hydrogen production by catalytic methane decomposition: carbon materials as catalysts or catalyst supports, Int. J. Hydrogen Energy 42 (2017) 19755–19775.
[13] W. Zhang, Q. Ge, H. Xu, Influences of precipitate rinsing solvents on Ni catalyst for methane decomposition to CO_x-free hydrogen, J. Phys. Chem. A 114 (2009) 3818–3823.
[14] L. Zhou, L.R. Enakonda, M. Harb, Y. Saih, A. Aguilar-Tapia, S. Ould-Chikh, J.-l. Hazemann, J. Li, N. Wei, D. Gary, Fe catalysts for methane decomposition to produce hydrogen and carbon nano materials, Appl. Catal. B 208 (2017) 44–59.
[15] Z. Guo, Z. Jia'E, Y. Liu, W. Chu, Insight into the role of metal/oxide interaction and Ni availabilities on NiAl mixed metal oxide catalysts for methane decomposition, Appl. Catal. A Gen. 555 (2018) 1–11.
[16] A.A. Ibrahim, A.H. Fakeeha, A.S. Al-Fatesh, A.E. Abasaeed, W.U. Khan, Methane decomposition over iron catalyst for hydrogen production, Int. J. Hydrogen Energy 40 (2015) 7593–7600.
[17] R.R. Silva, H.A. Oliveira, A.C. Guarino, B.B. Toledo, M.B. Moura, B.T. Oliveira, F.B. Passos, Effect of support on methane decomposition for hydrogen production over cobalt catalysts, Int. J. Hydrogen Energy 41 (2016) 6763–6772.
[18] P. Jana, V.A. de la Peña O'Shea, J.M. Coronado, D.P. Serrano, Co-production of graphene sheets and hydrogen by decomposition of methane using cobalt based catalysts, Energy Environ. Sci. 4 (2011) 778–783.
[19] M. Pudukudy, Z. Yaakob, Q. Jia, M.S. Takriff, Catalytic decomposition of undiluted methane into hydrogen and carbon nanotubes over Pt promoted Ni/CeO_2 catalysts, New J. Chem. 42 (2018) 14843–14856.
[20] A.C. Lua, H.Y. Wang, Decomposition of methane over unsupported porous nickel and alloy catalyst, Appl. Catal. B 132 (2013) 469–478.
[21] M. Pudukudy, Z. Yaakob, M.Z. Mazuki, M.S. Takriff, S.S. Jahaya, One-pot sol-gel synthesis of MgO nanoparticles supported nickel and iron catalysts for undiluted methane decomposition into CO_x free hydrogen and nanocarbon, Appl. Catal. B 218 (2017) 298–316.
[22] A.-C. Dupuis, The catalyst in the CCVD of carbon nanotubes—a review, Prog. Mater. Sci. 50 (2005) 929–961.
[23] D. Kang, J.W. Lee, Enhanced methane decomposition over nickel–carbon–B_2O_3 core–shell catalysts derived from carbon dioxide, Appl. Catal. B 186 (2016) 41–55.
[24] A. Rastegarpanah, M. Rezaei, F. Meshkani, K. Zhang, X. Zhao, W. Pei, Y. Liu, J. Deng, H. Arandiyan, H. Dai, Influence of group VIB metals on activity of the Ni/MgO catalysts for methane decomposition, Appl. Catal. B 248 (2019) 515–525.
[25] Y. Shen, A.C. Lua, Synthesis of Ni and Ni–Cu supported on carbon nanotubes for hydrogen and carbon production by catalytic decomposition of methane, Appl. Catal. B 164 (2015) 61–69.
[26] G.D.B. Nuernberg, H.V. Fajardo, E.L. Foletto, S.M. Hickel-Probst, N.L. Carreño, L.F. Probst, J. Barrault, Methane conversion to hydrogen and nanotubes on Pt/Ni catalysts supported over spinel $MgAl_2O_4$, Catal. Today 176 (2011) 465–469.
[27] A.E. Awadallah, A.A. Aboul-Enein, A.K. Aboul-Gheit, Various nickel doping in commercial Ni–Mo/Al_2O_3 as catalysts for natural gas decomposition to CO_x-free hydrogen production, Renew. Energy 57 (2013) 671–678.
[28] S. Takenaka, Y. Shigeta, E. Tanabe, K. Otsuka, Methane decomposition into hydrogen and carbon nanofibers over supported Pd–Ni catalysts, J. Catal. 220 (2003) 468–477.
[29] N.A. Hermes, M.A. Lansarin, O.W. Perez-Lopez, Catalytic decomposition of methane over M–Co–Al catalysts (M= Mg, Ni, Zn, Cu), Catal. Letters 141 (2011) 1018–1025.
[30] L. Avdeeva, O. Goncharova, D. Kochubey, V. Zaikovskii, L. Plyasova, B. Novgorodov, S.K. Shaikhutdinov, Coprecipitated Ni-alumina and Ni-Cu-alumina catalysts of methane decomposition and carbon deposition. II. Evolution of the catalysts in reaction, Appl. Catal. A Gen. 141 (1996) 117–129.
[31] Q. Chen, A.C. Lua, Kinetic reaction and deactivation studies on thermocatalytic decomposition of methane by electroless nickel plating catalyst, Chem. Eng. J. 389 (2020) 124366.
[32] H.S. Lim, D. Kang, J.W. Lee, Phase transition of Fe_2O_3–NiO to $NiFe_2O_4$ in perovskite catalytic particles for enhanced methane chemical looping reforming-decomposition with CO_2 conversion, Appl. Catal. B 202 (2017) 175–183.
[33] L.-S. Fan, L. Zeng, W. Wang, S. Luo, Chemical looping processes for CO_2 capture and carbonaceous fuel conversion – prospect and opportunity, Energy Environ. Sci. 5 (2012) 7254–7280.
[34] J.S. Zhang, V. Haribal, F.X. Li, Perovskite nanocomposites as effective CO_2-splitting agents in a cyclic redox scheme, Sci. Adv. 3 (2017) 8.
[35] T.L. Church, Y.D.Y.L. Getzler, C.M. Byrne, G.W. Coates, Carbonylation of heterocycles by homogeneous catalysts, Chem. Commun. (2007) 657–674.
[36] S.T. Gadge, B.M. Bhanage, Recent developments in palladium catalysed carbonylation reactions, RSC Adv. 4 (2014) 10367–10389.
[37] K. Ma, B.S. Martin, X. Yin, M. Dai, Natural product syntheses via carbonylative cyclizations, Nat. Prod. Rep. 36 (2019) 174–219.
[38] J. Zhang, V. Haribal, F. Li, Perovskite nanocomposites as effective CO_2-splitting agents in a cyclic redox scheme, Sci. Adv. 3 (2017) e1701184.
[39] L. Gama, M. Ribeiro, B. Barros, R. Kiminami, I. Weber, A. Costa, Synthesis and characterization of the $NiAl_2O_4$, $CoAl_2O_4$ and $ZnAl_2O_4$ spinels by the polymeric precursors method, J. Alloys. Compd. 483 (2009) 453–455.
[40] G. Kresse, J. Furthmüller, Efficient iterative schemes for ab initio total-energy calculations using a plane-wave basis set, Phys. Rev. B 54 (1996) 11169.
[41] G. Kresse, J. Furthmüller, Efficiency of ab-initio total energy calculations for metals and semiconductors using a plane-wave basis set, Comput. Mater. Sci. 6 (1996) 15–50.
[42] G. Kresse, J. Hafner, Ab initio molecular-dynamics simulation of the liquid-metal–amorphous-semiconductor transition in germanium, Phys. Rev. B 49 (1994) 14251.
[43] G. Kresse, J. Hafner, Ab initio molecular dynamics for liquid metals, Phys. Rev. B 47 (1993) 558.
[44] J.P. Perdew, K. Burke, M. Ernzerhof, Generalized gradient approximation made simple, Phys. Rev. Lett. 77 (1996) 3865.
[45] P.E. Blöchl, Projector augmented-wave method, Phys. Rev. B 50 (1994) 17953.
[46] G. Kresse, D. Joubert, From ultrasoft pseudopotentials to the projector augmented-wave method, Phys. Rev. B 59 (1999) 1758.
[47] H.J. Monkhorst, J.D. Pack, Special points for Brillouin-zone integrations, Phys. Rev. B 13 (1976) 5188.
[48] G. Henkelman, B.P. Uberuaga, H. Jónsson, A climbing image nudged elastic band method for finding saddle points and minimum energy paths, J. Chem. Phys. 113 (2000) 9901–9904.
[49] F. Birch, Finite elastic strain of cubic crystals, Phys. Rev. 71 (1947) 809.
[50] I.-K. Suh, H. Ohta, Y. Waseda, High-temperature thermal expansion of six metallic elements measured by dilatation method and X-ray diffraction, J. Mater. Sci. 23 (1988) 757–760.
[51] K. Persson, materials data on InNi2 (SG: 194) by materials project, LBNL Materials Project; Lawrence Berkeley National Laboratory (LBNL), (2016).
[52] J. Zhang, F. Li, Coke-resistant Ni@SiO_2 catalyst for dry reforming of methane, Appl. Catal. B 176 (2015) 513–521.
[53] X. Li, D. Li, H. Tian, L. Zeng, Z.-J. Zhao, J. Gong, Dry reforming of methane over Ni/La_2O_3 nanorod catalysts with stabilized Ni nanoparticles, Appl. Catal. B 202 (2017) 683–694.
[54] C. Montero, A. Ochoa, P. Castaño, J. Bilbao, A.G. Gayubo, Monitoring Ni0 and coke evolution during the deactivation of a Ni/La_2O_3–αAl_2O_3 catalyst in ethanol steam reforming in a fluidized bed, J. Catal. 331 (2015) 181–192.
[55] S. Chen, L. Zeng, H. Tian, X. Li, J. Gong, Enhanced lattice oxygen reactivity over Ni-modified WO_3-based redox catalysts for chemical looping partial oxidation of methane, ACS Catal. 7 (2017) 3548–3559.
[56] X. Gao, Y. Zhang, B. Li, Y. Zhao, B. Jiang, Determination of the intrinsic reactivities for carbon dioxide gasification of rice husk chars through using random pore model, Bioresour. Technol. 218 (2016) 1073–1081.
[57] L. Lin, M. Strand, Investigation of the intrinsic CO_2 gasification kinetics of biomass char at medium to high temperatures, Appl. Energy 109 (2013) 220–228.
[58] C. Dang, Y. Li, S.M. Yusuf, Y. Cao, H. Wang, H. Yu, F. Peng, F. Li, Calcium cobaltate: a phase-change catalyst for stable hydrogen production from bio-glycerol, Energy Environ. Sci. 11 (2018) 660–668.
[59] R. Watwe, H.S. Bengaard, J. Rostrup-Nielsen, J. Dumesic, J.K. Nørskov, Theoretical studies of stability and reactivity of CHx species on Ni (111), J. Catal. 189 (2000) 16–30.
[60] H. Liu, R. Zhang, R. Yan, B. Wang, K. Xie, CH4 dissociation on NiCo (1 1 1) surface: A first-principles study, Appl. Surf. Sci. 257 (2011) 8955–8964.
[61] P. Kratzer, B. Hammer, J. No/rskov, A theoretical study of CH4 dissociation on pure and gold-alloyed Ni (111) surfaces, J. Chem. Phys. 105 (1996) 5595–5604.
[62] K.G. Prasanna, R.A. Olsen, Á. Valdés, G.-J. Kroes, Towards an understanding of the vibrational mode specificity for dissociative chemisorption of CH_4 on Ni (111): a 15 dimensional study, J. Chem. Soc. Faraday Trans. 12 (2010) 7654–7661.